Efficient GRE Techniques for the Scattering of Three-Dimensional Arbitrarily Shaped Deep Cavities

Shumin Wang

Department of Electrical Engineering, The Ohio State University,
1320 Kinnear Road, Columbus, OH 43212, U.S.A
Email: james.wang@ieee.org

Mingzhi Li, Changqing Wang and Xili Zhu

Department of Electronics, Beijing University, Beijing, 100871, P. R. China

ABSTRACT: An efficient implementation of the Generalized Ray Expansion (GRE) method for computing the scattering of three-dimensional (3-D) arbitrarily shaped deep cavities is studied in this paper. Efficiency is being sought from two aspects: ray racing in discrete cavities and reflection from individual patches. An improved algorithm for detecting intersections between a ray and triangular patches has been proposed, which is about 2.83 times faster than the traditional algorithm. Also, sectional algorithm and Wavefront Advancing and Candidate Narrowing (WACN) algorithm for tracing rays inside 3-D cavities are proposed to boost efficiency. As to reflection from individual patches, different local cavity reconstruction methods are being tested and interpolative triangular patches are found to be an efficient choice. Finally, several numerical examples further demonstrate the versatility and validity of our approach.

I.   INTRODUCTION

Electromagnetic scattering from arbitrarily shaped deep cavities is of great importance in radar cross section (RCS) estimation of modern jet aircraft [1]-[8]. Because these targets are usually composed of two different parts, i.e., an electrically large, smooth varying air duct and a relatively short, geometrically complex termination, methods suitable for one part generally become unsuitable or even fail for the other part. Due to this discrepancy, hybrid methods are often used instead to solve for different parts [8]. In this article, we shall focus on efficient computation of the electrically large, smooth varying air duct. The methods involved generally include differential equation-based methods [7], integral equation-based methods, waveguide modal analysis and high frequency asymptotic methods [3]. Differential equation- and integral equation-based methods are accurate while much less efficient for deep cavity problems due to the prohibitive amount of memory and CPU requirements. Furthermore, differential equation-based methods suffer from numerical dispersion error for electrically large

problems and their applications to deep cavity scattering are limited. Waveguide modal analysis also provides accurate results [3], [4], but the exact waveguide eigenmodes have only been found for simple cross sections. These methods are most often used to give reference solutions.

Because of the smooth varying property of the air duct required by aerodynamics, ray and beam techniques are usually used for high frequency asymptotic methods. The early version was the Shooting and Bouncing Ray (SBR) method which utilizes Geometric Optics (GO) for ray tracing and Aperture Integration (AI) or Reciprocal Integral (RI) for far field computations [1]-[4], [6]. The major problem with the SBR method is that it does not consider higher order effects -especially the field diffracted into the cavity by the rim of the open end. Thus it generally provides an envelope but not details of the scattering pattern. Gaussian Beam (GB) is another approach which instead traces Gaussian beams [3], [5]. Since the Gaussian beam is caustic free by its nature and because it considers fields diffracted into the cavity from the open end, it has much better accuracy than the SBR method. But the beam distortion after a few reflections generally prevents this method from deep cavity problems. The GRE method could be thought of as a combination of SBR and GB methods in some sense [3]. Based on the sub-aperture expansion techniques of the GB method, the GRE method traces GO rays instead of Gaussian beams to improve the beam distortion problem. Since the GRE method includes the interior diffraction by the edge of the open end, it is also more accurate than the SBR method.

The usage of the GRE method is limited by the necessity of tracing massive amounts of rays. This is in turn related to the modeling of a cavity. For simple geometry, analytical functions could be used thus ray tracing is obviously not a problem. For realistic large and arbitrarily shaped cavities, modeling a cavity with ordered 3-D discrete points, which could either be the results of physical measurements or generated by CAD software, is of great versatility and generality.

When applying GRE methods to such realistic 3-D *discrete* cavities, two essential issues need to be

considered. The fist issue is fast ray tracing algorithms in 3-D *discrete* cavities. This topic is rarely documented because most 3-D ray tracing algorithms are designed for 3-D bodies. We shall solve this problem from two aspects: fastening the intersection test of a ray and a triangular patch and reducing the total number of such test needed. An improved intersection test algorithm is proposed for the first aspect and two other algorithms, a sectional algorithm for general cavities and a WACN algorithm for convex cavities, are proposed for the second aspect. The second issue is local cavity reconstruction. There are quite a few choices ranging from simple triangular patches to complex Hermitian bicubic patches. We shall study the accuracy of using different reconstruction methods for reflection computation. We found that an interpolative triangular patch, which is simple to implement and highly accurate, was the best choice.

This article is organized as follows: Section II briefly introduces the GRE method. Section III discusses the efficiency issues. Section IV provides numerical examples. Finally, some conclusions are drawn in Section V.

II.   GRE METHOD

In the GRE method, the open end of the cavity is divided into multiple sub-apertures. The electric field radiated by the n-*th* sub-aperture is determined by far zone Kirchhoff approximation with the cavity wall absent. Cone-shaped angular grids of ray-tube are launched from the center of each sub-aperture to represent the spherical wave entering into the cavity. By assuming a local plane wave at the open end and using Physical Optics (PO) to obtain the equivalent electric and magnetic currents, the electric field of the p-*th* ray-tube of the n-*th* sub-aperture is expressed as

$$
\begin{aligned}
\vec{E}_n\left(\vec{r}_n^{\,p}\right) = &-\frac{jk}{4\pi}\frac{e^{-jkr_n^p}}{r_n^p}\{\iint_{S_n} \hat{r}_n^p \times [\hat{s}_n' \times \vec{E}_i(\vec{r}_n')]e^{jk\vec{r}_n'\cdot\vec{r}_n^p}\,dS' \\
&-Z_0\cdot\hat{r}_n^p \times \iint_{S_n} \hat{r}_n^p \times [s_n' \times \vec{H}_i(\vec{r}_n')]e^{jk\vec{r}_n'\cdot\vec{r}_n^p}\,dS'\} \\
=&\ \frac{e^{-jkr_n^p}}{r_n^p}\vec{F}_n(\hat{r}_n^p,\vec{E}_i)
\end{aligned}
$$

$$(1)$$

where k is the wave number, $\vec{r}_n^{\,p} = r_n^p \hat{r}_n^p$ and $\hat{r}_n^p$ is the unit vector representing the direction of the p-*th* ray-tube, $\vec{r}_n'$ represents the location of an equivalent source on the sub-aperture, $\hat{s}_n'$ is the unit surface normal pointing inwards the cavity, and $\vec{E}(\vec{r})$ and $\vec{H}(\vec{r})$ represent the incident electric and magnetic field respectively. The integration is over the sub-aperture. Note that the far zone radiating field is decomposed

into the product of a spherical wave and a vector far zone pattern. Portions of the spherical wave could be individually traced as GO rays. Incident field information is only contained in the vector far zone pattern $\vec{F}_n(\hat{r}_n^p,\vec{E}_i)$. Ray tracing and the calculation of $\vec{F}_n(\hat{r}_n^p,\vec{E}_i)$ are independent. Thus the GRE method could generate the result at any incident angle in the effective angular range ($10^o - 15^o$ narrower than the largest ray tracing angle) with just one ray tracing. Also, ray tracing is time consuming rather than memory consuming. The independency of each ray tracing makes it very suitable to utilize distributed computer systems because there are virtually no communications between different processes and load balancing is easy to handle.

The total transmitted field could be written as

$$
\vec{E}\ (\vec{r}) = \sum_{n=1}^{N}\sum_{p=1}^{P}\vec{E}_n^{\,p}(\vec{r}_n^{\,p}) \tag{2}
$$

To evaluate $\vec{F}_n(\hat{r}_n^p,\vec{E}_i)$, we first express the incident field as

$$
\vec{E}_i(\vec{r}_n') = \vec{p}_e E_i(\vec{r}_n') \tag{3}
$$

$$
\vec{H}_i(\vec{r}_n') = \vec{p}_h H_i(\vec{r}_n') = \vec{k}_i \times \vec{E}_i(\vec{r}_n')/Z_0
$$

where $\vec{p}_e$ and $\vec{p}_h$ represent the directions of the incident electric and magnetic field respectively and Z_0 is the free space wave impedance. Establishing a local coordinate system, say Γ', originating at the center of a sub-aperture and in which $\hat{e}_x, \hat{e}_y$ are any two orthogonal unit vectors tangential to the sub-aperture, and in which $\hat{e}_z$ points into the cavity, $\vec{F}_n(\hat{r}_n^p,\vec{E}_i)$ could be decomposed into $\hat{\theta}$ and $\hat{\phi}$ polarization

$$
\vec{F}_n(\hat{r}_n^p,\vec{E}_i) = F_{n\theta}(\hat{r}_n^p,\vec{E}_i)\hat{\theta}_n + \vec{F}_{n\phi}(\hat{r}_n^p,\vec{E}_i)\hat{\phi}_n \tag{4}
$$

with

$$
\begin{aligned}
\vec{F}_{n\theta}(\hat{r}_n^p,\vec{E}_i) = &[(p_{ex}+p_{hy}\cos\theta_n^p)\cos\phi_n^p + \\
&(p_{ey}-p_{hx}\cos\theta_n^p)\sin\phi_n^p]I(\hat{r}_n^p,\vec{E}_i)
\end{aligned} \tag{5}
$$

$$
\begin{aligned}
\vec{F}_{n\phi}(\hat{r}_n^p,\vec{E}_i) = &[(p_{ey}\cos\theta_n^p - p_{hx})\cos\phi_n^p - \\
&(p_{hy}+p_{ex}\cos\theta_n^p)\sin\phi_n^p]I(\hat{r}_n^p,\vec{E}_i)
\end{aligned} \tag{6}
$$

where θ_n^p and ϕ_n^p represent the elevation and azimuth angles of the axis of the *p-th* ray-tube of the *n-th* sub-aperture, measured in the local coordinate system Γ', p_{ex} and p_{ey} are the components of $\vec{p}_e$ in Γ' and similar for p_{hx} and p_{hy}. The exact form of $I(\hat{r}_n^p,\vec{E}_i)$ relies on the shape of the sub-aperture (see Ref. [3]).

Rays are bounced back and forth inside the cavity. After each reflection, the magnitude is determined by

$$\vec{E}(\vec{r}_i) = [R] \cdot \vec{E}(\vec{r}_{i-1}) \cdot [DF]_{i-1} e^{-jks} \qquad (7)$$

where $\vec{r}_i$ is the location of the i-*th* reflection, $s = |\vec{r}_i - \vec{r}_{i-1}|$, [DF]$_{i-1}$ is the divergence factor at the (i-1)-*th* reflection location, [R] is the reflection matrix of the cavity wall which could be written in the PEC case as

$$\vec{E}^r = \begin{bmatrix} E_\perp^r \\ E_{//}^r \end{bmatrix} = [R] \cdot \vec{E}^i = \begin{bmatrix} -1 & 0 \\ 0 & 1 \end{bmatrix} \cdot \begin{bmatrix} E_\perp^i \\ E_{//}^i \end{bmatrix}$$

where superscripts *r* and *i* denote the reflected and incident wave respectively, and where $\perp$ and // represent the perpendicular and parallel polarization. When a cavity is coated with materials, the impedance boundary condition could be used casually instead of the PEC boundary condition. Easy manipulation of boundary conditions is another advantage of ray-based techniques over other methods. The divergency factor is determined by *s* and the principal radii of the curvature of the wavefront, say R_1 and R_2, at $\vec{r}_{i-1}$

$$[DF]_{i-1} = \frac{1}{\sqrt{1 + s/R_1}} \cdot \frac{1}{\sqrt{1 + s/R_2}} \qquad (8)$$

Note that the reflection field is singular if the i-*th* reflection is located at the caustics, i.e., $s = -R_1$ or $s = -R_2$. The caustic problem is inherent to all GO-based techniques. When it occurs, we chose to abandon the ray being traced for efficiency considerations.

Rays could exit from either the front end or the rear end. In the first case, the far zone scattering field is determined by the AI method. In the second case, RI could be used to calculate the far field contribution of a ray tube directly without tracing it back. Without wall losses, the cross section area of the reflected ray-cube, say *S*, could be determined via energy conservation by

$$S_0 |\vec{E}_0|^2 = S |\vec{E}|^2 \qquad (9)$$

where S_0 is the initial beam solid angle of the ray-tube.

III. EFFICIENCY IMPROVEMENTS

The major thrust of the GRE method is to trace massive amounts of ray-tubes inside an arbitrarily shaped cavity. Usually, 10^5 - 10^6 rays are expected; however, if the axial length of the cavity is about 100λ, this number could reach 10^7 - 10^8. Therefore, ray tracing efficiency is of paramount importance.

Ray tracing is essentially a computer graphics topic. In our context, its efficiency is determined rather by the accuracy of scattering field computation than by the quality of graphic displaying. We can further divide the ray tracing problem into two weakly coupled problems: determination of the reflection position and computation of the reflected field. In general, when we calculate a GO ray reflection, we need to reconstruct the local cavity from those discrete points surrounding the reflection point. For a fixed set of discrete points, if their is a better way to reconstruct the local surface so that the resultant reflection calculation is more accurate, we can use less discrete points to model the cavity. The efficiency of determining the reflection position in a discrete cavity is essentially dominated by the number of discrete points being used to describe the cavity. Thus these two problems are weakly coupled in this sense. In general, we can improve the overall efficiency by working on each problem individually.

A. Ray Tracing

Ray tracing involves finding the reflection of a ray-tube. During each ray tracing, triangular patches were used to determine the reflection position, though in some cases as a preliminary step. Basic ray tracing algorithms include two procedures: 1) Determination of possible intersections of a ray and all triangular patches; 2) Sorting the distance between the current position and all possible intersections. The shortest distance corresponds to the actual reflection. We attempt to improve the efficiency of each procedure in the following.

A.1 Determine Intersections

The traditional way to determine a possible intersection starts from calculating the intersection of a ray and the plane where a triangular patch is located [9]. Considering a ray originating at (x_0, y_0, z_0) and shooting towards (k_x, k_y, k_z), the ray function is written as

$$x = k_1(z - z_0) + x_0, \quad y = k_2(z - z_0) + y_0$$

with $k_1 = k_x/k_z$ and $k_2 = k_y/k_z$. This requires two multiplications and four summations (we do not consider those operations solely related to the ray function because they are performed only once for a ray but not for all triangular patches being tested.). The plane function of a triangular patch, written as $ax + by + cz + d = 0$, could be determined by the coordinates of its three vertices by solving a set of inhomogeneous linear equations, which requires 36 multiplications/divisions and 20 summations. The solution of the intersection needs additional seven multiplications/divisions and six summations. Next, the intersection is tested to determine whether it is inside the triangular patch or not. We adopt the following scheme: 1) Three vectors were constructed by connecting three vertices to the intersection. This requires nine summations. 2) All cross products between any two of the three vectors were gathered. This requires 18 multiplications and nine summations.

3) All dot products of any two vectors obtained in step two were obtained. This requires nine multiplications and six summations. If the intersection is inside the triangular patch, all cross products must be in the same direction if being calculated with a certain circulation order. Otherwise, their must be one cross product with a sign different from the others. In fact, if we find that two dot products have different signs, we can reach a conclusion immediately. This step requires 27 multiplications and 24 summations in the worst case. Thus in the traditional method, totally 72 multiplications/divisions and 64 summations are needed in the worst case (136 flops).
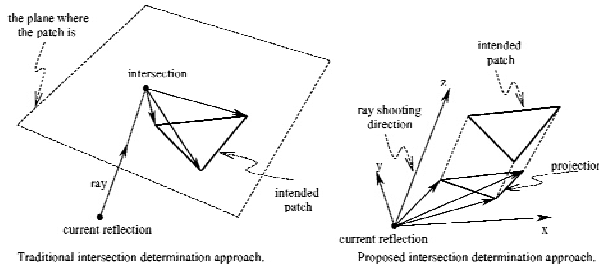
Fig. 1. Comparison of traditional and proposed intersection determination approaches.

The key to efficiency improvements is to bring 3-D operations to two-dimensional (2-D) operations. To do so, we first project the three vertices of a triangular patch onto the x-y plane of another coordinate system originating at (x_0, y_0, z_0) and whose z-axis coincides with the direction of the ray. This requires 18 multiplications and 21 summations. Then all cross products between any two of three 2-D vectors obtained in the first step are calculated. If the intersection is inside the triangular patch, all three cross products must be of the same sign when being calculated with a certain circulation order. Otherwise, their must be one cross product with a sign different from the others. This step requires six multiplications and three summations. Therefore, the proposed scheme requires a total of 24 multiplications and 24 summations (48 flops). Compared with the traditional approach, this algorithm needs 35% less flops and hence is 2.83 times faster. Moreover, this algorithm is more accurate and robust because it does not involve any division operation.

A.2   Ray Tracing In Cavities

As has already been pointed out, the heart of any ray tracing algorithm is sorting and the key to efficiency improvements is exploiting data coherence [9], [10]. An efficient algorithm is typically achieved by avoiding expensive intersection computation as much as possible and by sorting the least possible amount of intersections or no such sorting at all. If all 3-D discrete points are given without any coherence, it would be hard to improve the efficiency.

Let us assume that all discrete points are given in m consecutive cuts along the z-axis and let us call them z-cut. Discrete points in one z-cut form a polygon (z-polygon) and those in adjacent cuts form a section of the cavity when connected. The whole cavity is formed by (m -1) such sections, e.g. Fig.5 and Fig.6. With this model, we can search for the next reflection section by section from where the current reflection is and along either positive or negative z-directions, depending on the direction of the ray. In this manner, the first intersection must be the actual reflection and no sorting is needed at all. We call this method the sectional algorithm.

In fact, 3-D discrete points are either specified by physical measurement or generated by CAD software. It would be natural to require them to be generated in the above manner. For those models which are different and can not be regenerated, we may run a pre-processing program to reform them. In the following, we shall assume that such a model is always available.

The sectional algorithm totally avoids sorting, but the number of intersection computations could still be large. We can further improve the performance for convex cavities with the following Wavefront Advancing and Candidate Narrowing (WACN) algorithm. This algorithm starts from computing the intersection of a ray and a z-cut and determining whether the intersection is inside the z-polygon. If the intersection is out of the current z-polygon but is inside the previous z-polygon, it must be reflected by the section formed by these two z-polygons. To test whether an intersection is inside a z-polygon, we need to specify a gauge point for each z-polygon. To understand the role of gauge points, we notice that any 2-D line (formed by adjacent vertices of a z-polygon) divides a 2-D space (or hyper plane) into two half-spaces. When all points in one half-space are substituted into the line equation, the results must bear the same sign [10]. If the line equation is adjusted such that any point from the interior of the polygon yields a positive (or negative) sign when being substituted into the line equation, we can determine whether an intersection is inside a z-polygon or not. A gauge point serves this purpose and it could be any point inside a z-polygon. A 2-D line equation $ax + by + cz + d = 0$ could be solved by the coordinates of its two vertices with six multiplications/divisions and three summations. The gauging and the determination procedures totally require four multiplications and four summations. Thus for one possible triangular patch, ten multiplications/divisions and seven summations (17 flops) are required. This is about 35% of the proposed intersection tests needed. Since the current wavefront

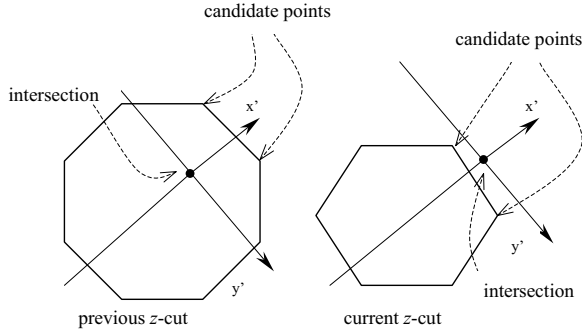advances consecutively, we call it Wavefront Advancing.

Fig. 2. The local coordinate systems and candidate points that the candidate triangular patch must contain.

If a reflection is about to happen in a section, the candidate triangular patches which are possible for actual reflection could be further narrowed down. This is accomplished through the following steps: 1) In the previous z-cut (where the intersection is inside the z-polygon), construct a Cartesian coordinate system whose x'-axis is the projection of the ray on the z-cut and whose y'-axis is perpendicular to the x'-axis. 2) Transform all vertices of the z-polygon to this new coordinate system and *only* compute their y' components. 3) Check the signs of all y' components consecutively. If two adjacent y' components are of opposite sign, record their indices. 4) Calculate the x' components of the two pairs of points obtained in step three. The candidate triangular patch must contain the pair of points which both have positive x' components. 5) Repeat steps one to three for the current z-cut (where the intersection is out of the z-polygon). 6) Calculate the x' components of the two pairs of points obtained in step five. The candidate triangular patch must contain the pair of points closest to the x'-axis. After the above steps, only those triangular patch (not necessarily two patches) containing the two pairs of points in the current and previous z-cuts are possible for the actual reflection. The candidate triangular patches are narrowed down and we call this step Candidate Narrowing. Note that obtaining either the x' components or the y' components only requires two multiplications and one summation, thus expensive intersection tests are replaced by these simple operations.

B.   Elementary Reflection

In this subsection, the effect of using different cavity reconstruction methods for computing the reflection will be discussed.
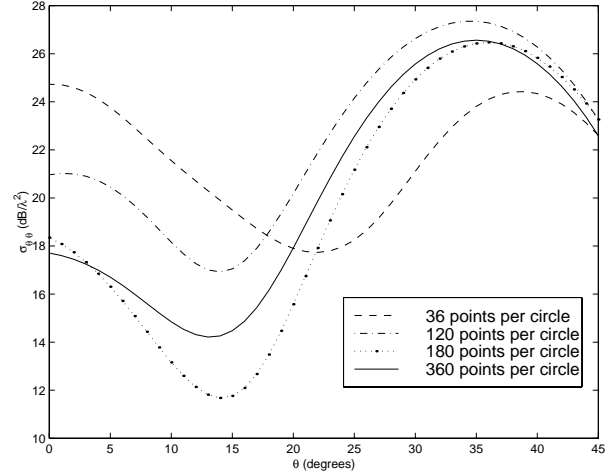

Fig. 3. Convergence of simple triangular patches for $\sigma_{\theta\theta}$ of $3\lambda \times 9\lambda$ circular waveguide.
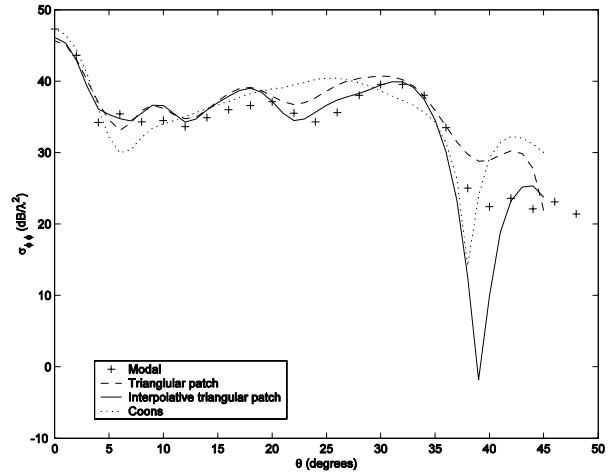

Fig. 4. $\sigma_{\varphi\varphi}$ of $10\lambda \times 10\lambda$ circular waveguide calculated by using different reconstruction methods.

B.1   Simple Triangular Patch

In this approach, each triangular patch is considered as a simple plane. Since the principal radii are infinite, the caustic problem does not exit. In general, more triangular patches should be used if better accuracy is required. To study the convergency, we calculate the $\theta\theta$ polarized mono-static RCS of a circular waveguide. The waveguide is of 3λ in diameter and 9λ in length. Different numbers of triangular patches per section, which are in turn represented by the number of discrete points per circle, is being used. The results are shown in Fig.3. We observe that when only 36 points per circle (72 patches per section) are used, there are significant errors for all angles. As the number of patches is increased, the performance improves and 180 points per circle yields errors within 3dB/ λ^2 compared with 360 points per circle. Fig.4 shows the $\varphi\varphi$ polarized mono-static RCS of a circular waveguide of 10λ in diameter and 10λ in length. 180 points per circle are used for

reconstruction by simple triangular patches. Ray tracing is confined within 45° and the effective angle is up to 30° - 35° according to theory [3]. It is observed that the results agree with those obtained by Modal analysis well up to 35°.

Using more triangular patches makes ray tracing less efficient. In the following, we shall explore other possibilities with better performances.

B.2   Coons Patch

Since the inaccuracy with simple triangular patches is caused by the assumption of infinite principal radii, it is natural to consider using surfaces with curvature. Here we choose Coons patch. The Coons patch belongs to the family of Hermitian bicubic parametric patches. It only uses the information on its four corners to determine the parameters. To further introduce this method, let us denote a Coons patch with two parameters (u, v) as $R(u, v) = \{x(u, v),\ y(u, v),\ z(u, v)\}$, with $0 \leq u \leq 1$ and $0 \leq v \leq 1$. If uv is used as an abbreviation for $R(u, v)$, then 00, 01, 10, 11 represent the four corners respectively; 00_u, 01_u, 10_u, 11_u, 00_v, 01_v, 10_v, 11_v represent the first order tangential derivatives at each corner; and 00_{uv}, 01_{uv}, 10_{uv}, 11_{uv} represent the second order tangential derivatives at each corner, which are also called *twists*. A Coons patch is then expressed as

$$uv = (u^3, u^2, u, 1) \cdot [H] \cdot [M] \cdot [H]^T \cdot (v^3, v^2, v, 1)^T$$
(10)

where

$$[M] = \begin{bmatrix} 00 & 01 & 00_v & 01_v \\ 10 & 11 & 10_v & 11_v \\ 00_u & 01_u & 00_{uv} & 01_{uv} \\ 10_u & 11_u & 10_{uv} & 11_{uv} \end{bmatrix}$$

$$[H] = \begin{bmatrix} 2 & -2 & 1 & 1 \\ -3 & 3 & -2 & -1 \\ 0 & 0 & 1 & 0 \\ 1 & 0 & 0 & 0 \end{bmatrix}$$

Other options for bicubic surfaces include Bézier surface and B-spline surface. They differ from Coons patch primarily by the meaning of [M] and the form of [H]. Since they are more often used in interactive graphic design, we shall not consider them here.

The great advantage of the Coons patch (as with other Hermitian patches) is that when two adjacent Coons patches are constructed separately, the first order continuity (C^1 continuity) across the patch edges is guaranteed. Thus we can construct a Coons patch whenever needed without considering the global C^1 continuity. Compared with triangle patches, which are

of C^0 continuity, C^1 continuity is preferred in computer graphics because of more realistic results.

On the other hand, the Coons patch is a cubic function of each of its parameter u and v. This property causes unnecessary surface twists and it is disadvantageous when being used to calculate the reflection and the divergence factor $[DF]_i$. Fig.4 shows the $\varphi\varphi$ polarized mono-static RCS of a 10λ x 10λ circular waveguide calculated by using Coons patches with 36 points per circle. We observe that except for the main lobe, the results roughly deviate from the reference values the most.

To find the exact reflection position, we need to solve a set of linear and non-linear equations including Eq. (10) and the ray function. If the Newton iterative method is used, three to four iterations should be expected with good initial guesses and appropriate accuracy control. This procedure consumes more CPU time than the computation of the reflection field itself.

B.3   Interpolative Triangular Patch

In this approach, the reflection position is determined by treating a triangular patch as a simple plane. To compute the reflection direction and the divergence factor $[DF]_i$, the triangular patch is assumed to have curvature. Its first and second order derivatives at the reflection position are obtained by linear interpolation of those at the vertices. Compared with the Coons patch, this approach not only eliminates surface twists, but also simplifies the calculation of the reflection.

Fig.4 also depicts the $\varphi\varphi$ polarized mono-static RCS of a 10λ x 10λ circular waveguide calculated by using interpolative triangular patches with 36 points per circle. As can be seen, the results are much better than those for Coons patches with the same amount of points per circle and agree with the reference values the best (within effective angle 35°). Compared with that of simple triangular patches, the consideration of curvature improves the accuracy to higher degree at large angles (20° above) than at small angles. Bearing in mind that the improvements are obtained by using 20% discrete points, as in the case of simple triangular patches, we consider this as our best choice.

IV.   NUMERICAL EXAMPLES

Besides the example shown in Fig.4 as a verification of our approach, we further show some more realistically shaped examples to demonstrate the versatility. The first example is a PEC cavity with a slanted front end. The cavity is formed by six sections. The first section is a slanted aperture of 10λ in length. The angle between the normal to the aperture, i.e. $\hat{n}$, and the z-axis, is 45°. The angle between the plane, in which $\hat{n}$ and the z-axis are located, and the x-axis is 0°.

The second section is 10λ in length and its cross section is a square with side lengths of 10λ. The third section is a 6.7λ transition region where the cross section changes from a square with a side length of 10λ to a circle of 10λ in diameter. The fourth section is 8.3λ in length and its cross section is a circle of 10λ in diameter. The fifth section is another transition region of 8.3λ in length and its cross section changes from a circle of 10λ in diameter to a circle of 8λ in diameter. The final section is of 6.7λ in length and its cross section is a circle of 8λ in diameter. The geometry is shown in Fig.5 with adjusted axial ratios. The side view is shown in Fig.7 with real axial ratios. All figures are in the unit of wavelength.
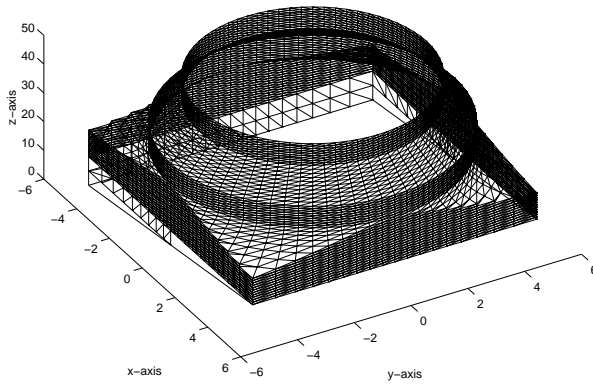
Fig. 5. Cavity with slanted front end.
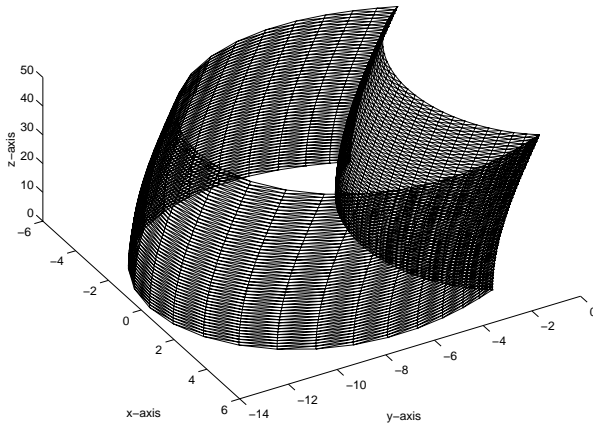
Fig. 6. Cavity with axial lofting.

For comparison, we built another model with a normal front end. The only difference is that the first section has the same cross section as the second section, i.e. the front end is perpendicular to the z-axis. Both cavities are terminated with simple PEC plates.

We use interpolative triangular patches to reconstruct the cavity with 72 points per cross section and WACN algorithm for ray tracing. Fig.9 and Fig.10 show that both θθ and φφ polarized RCS at φ = 0°. θ takes a

positive sign when an observation has a positive *x* coordinate and negative sign otherwise. As we see, the main lobes of σ_{θθ} and σ_{φφ} of the cavity with normal front end do not occur at the normal incidence but at some larger angles. When the front end becomes slanted, the main lobe is close to the normal incidence but shifts slightly towards negative θ direction.
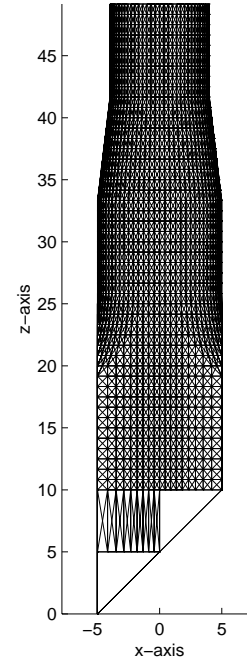

Fig. 7. Side view of the cavity with slanted front end.

Note that the results for the cavity with normal front end are not exactly symmetrical. This is due to the low grid density (eight points per λ) being used in aperture integration. The results converge slowly to symmetrical forms if grid density becomes denser. Without exception, all aperture integration in this section will be performed with the above grid density.

The second example is a concave cavity with axial lofting as shown in Fig.6 with adjusted axial ratios. A side view with real axial ratios is depicted in Fig.8. The axis is described by the following function with *z* as a parameter

$$x = 0, \qquad y = 2(\lambda - \cos(\pi z / 100\lambda))$$

Each cross section is formed by two parts. The shorter one is an arc of a circle of 5λ in radius. The longer one is described by a curve $5\lambda(\sqrt{3\lambda - \sin^2 \psi} + \cos\psi)$ with $4\pi/3 \leq \varphi \leq 8\pi/3$. Both are centered at the axis. The cavity is also terminated by a PEC plate.

We use interpolative triangular patches to reconstruct the cavity with 24 points per arc, and sectional algorithm for ray tracing. Fig.11 and Fig.12 reveal that the RCS of θθ and φφ polarization at φ = 0° and φ = 90°. At φ = 0°, θ takes a positive sign when an observation has a positive *x* coordinate and a negative

sign otherwise. A similar convention holds at $\varphi = 90^{\circ}$. The RCS at $\varphi = 0^{\circ}$ has main lobes at normal incidence. The weak asymmetry is also caused by insufficient grid density in aperture integration. At $\varphi = 90^{\circ}$, the main lobes of both polarization shift toward the negative direction. This corresponds to the direction where the termination could be illuminated directly. Note that there are actually two main lobes for the $\theta\theta$ polarization and its scattering is much stronger than that of the $\varphi\varphi$ polarization.
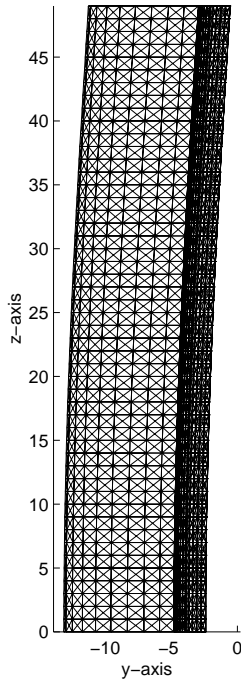

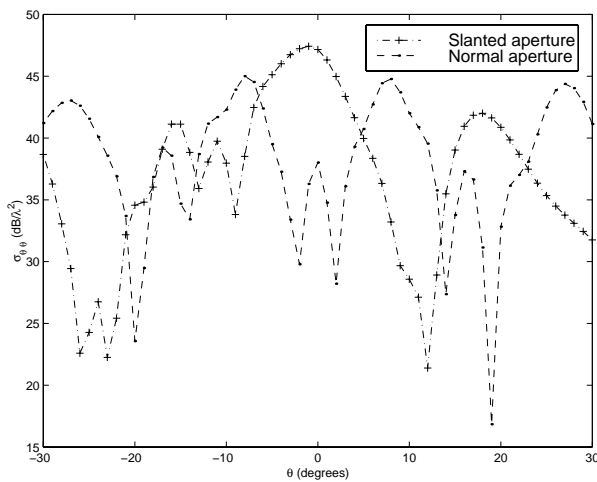Fig. 8. Side view of the cavity with axial lofting.

Fig. 9. Comparison of $\sigma_{\theta\theta}$ at $\varphi = 0^{\circ}$ of cavities with slanted and normal aperture.
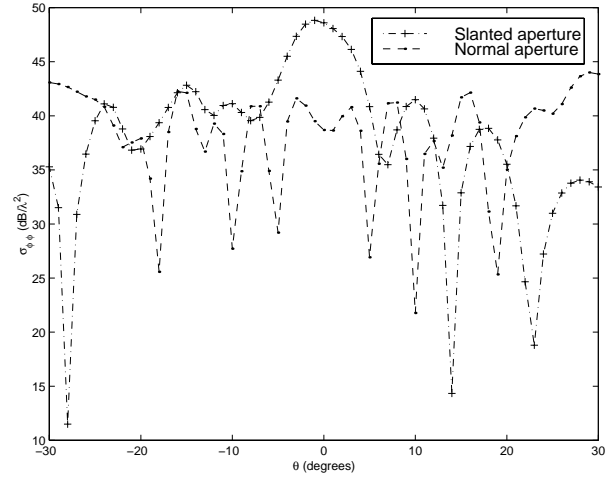

Fig. 10. Comparison of $\sigma_{\varphi\varphi}$ at $\varphi = 0^{\circ}$ of cavities with slanted and normal aperture.
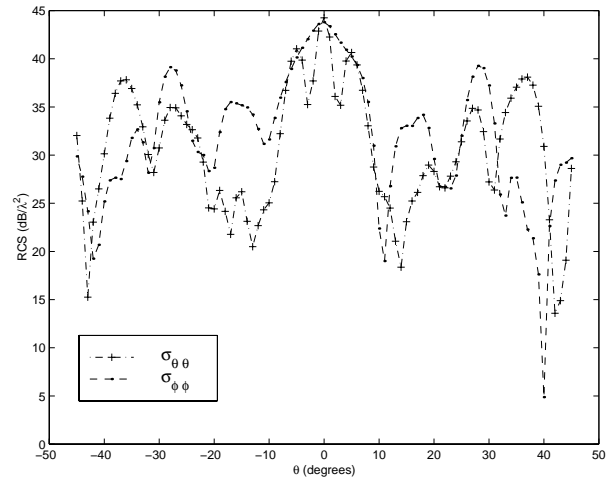

Fig. 11. $\sigma_{\theta\theta}$ and $\sigma_{\varphi\varphi}$ at $\varphi = 0^{\circ}$ of the cavity with axial lofting.
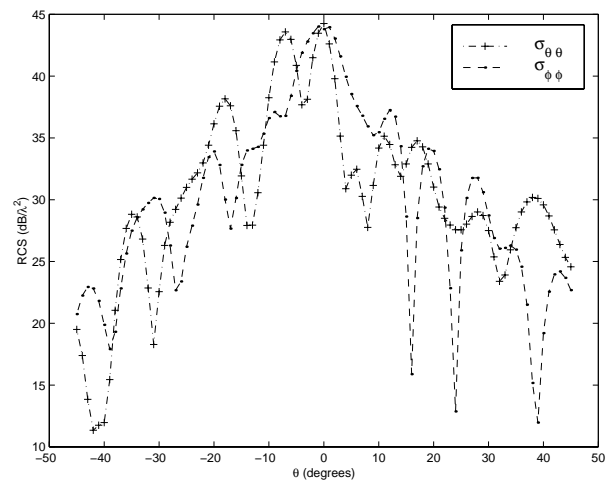

Fig. 12. $\sigma_{\theta\theta}$ and $\sigma_{\varphi\varphi}$ at $\varphi = 90^{\circ}$ of the cavity with axial lofting.

V.   CONCLUSION

In this article, we have discussed several efficiency considerations of the GRE method for computing electromagnetic scattering from 3-D arbitrarily shaped deep cavities. An improved algorithm for testing the intersection of a ray and a triangular patch is proposed, which is 2.83 times faster than the traditional approach. Two efficient algorithms for ray tracing in 3-D discrete cavities - the sectional algorithm and the WACN algorithm - are also proposed. The WACN algorithm further boosts the efficiency by 2.83 times for convex cavities. The effects of using different reconstruction methods are explored. Numerical examples further show the validity and versatility of our approaches. Future work should address the implementation of these approaches on distributed computer systems.

REFERENCES:

[1] H. Ling, R. Chou and S. W. Lee *Shooting and Bouncing Rays: Calculating the RCS of an Arbitrarily Shape Cavity*, IEEE Trans. AP-37(2), pp.194-205, 1989.

[2] H. Ling, S. W. Lee and R. Chou *High Frequency RCS of Open Cavities with Rectangular and Circular Cross Sections*, IEEE Trans. AP-37(5), pp.648-654, 1989.

[3] R. J. Burkholder *High Frequency Asymptotic Methods for Analyzing the EM Scattering by Open-Ended Waveguide Cavities*, Ph.D. dissertation, The Ohio State Univ., 1989.

[4] P. H. Pathak and R. J. Burkholder *Modal, Ray, and Beam Techniques for Analyzing the EM Scattering by Open-Ended Waveguide Cavities*, IEEE Trans. AP-37 (5), pp.635-647, 1989.

[5] R. J. Burkholder and P. H. Pathak *Analysis of EM Penetration into and Scattering by Electrically Large Open Waveguide Cavities Using Gaussian Beam Shooting*, IEEE Proceedings. 79 (10), pp.1401-1412, 1991.

[6] P. H. Pathak and R. J. Burkholder *A Reciprocity Formulation for the EM Scattering by an Obstacle Within a Large Open Cavity*, IEEE Trans. MTT-41(4), pp.702-707, 1993.

[7] J. Liu and J. Jin *A Special Higher-order Finite Element Method for Scattering by Large Cavities*, IEEE AP-S Int. Symp., vol. 2, pp.1168 -1171, 2000.

[8] R. Lee and T-T Chia *Analysis of Electromagnetic Scattering from a Cavity with a Complex Termination by means of a Hybrid Ray-FDTD Method*, IEEE Trans. AP-41(11), pp.1560-1569, 1993.

[9] J. D. Foley, A. van Dam, S. K. Feiner and J. H. Hughes *Computer Graphics: Principals and Practice*, Addison Wesley, 2001.

[10] Z. Lou and G. Liao *Principles and Methods of Computer Graphics*, Fudan University Press, 1995.

Shumin Wang received the B.S. degree in physics from Qingdao University, P.R.China, and the M.S. degree in electronics from Beijing University, P.R.China, in 1995 and 1998 respectively. He is currently working towards the Ph.D. degree in electrical engineering at The Ohio State University. Since 1999, he has been a Graduate Research Associate with the ElectroScience Laboratory (ESL), The Ohio State University. His research interests include electro-static and magneto-static lens design, time-domain differential equation-based methods, high frequency asymptotic methods and their applications to scattering, packaging, microwave circuit and antenna analysis.